

# Phonon spectrum, thermodynamic properties, and pressure-temperature phase diagram of uranium dioxide

Bao-Tian Wang,<sup>1,2,3,\*</sup> Ping Zhang,<sup>2,†</sup> and Olle Eriksson<sup>3,‡</sup>

<sup>1</sup>*Institute of Theoretical Physics and Department of Physics, Shanxi University, Taiyuan 030006, People's Republic of China*

<sup>2</sup>*LCP, Institute of Applied Physics and Computational Mathematics, Beijing 100088, People's Republic of China*

<sup>3</sup>*Department of Physics and Astronomy, Division of Materials Theory, Uppsala University, Box 516, SE-75120 Uppsala, Sweden*

We present a study of the structural phase transition, mechanical and thermodynamic properties of  $\text{UO}_2$  by means of the local density approximation (LDA)+ $U$  approach. A phase transition pressure of 40 GPa, which agrees well with the experimental value of 42 GPa, is obtained from theory at 0 K. Pressure-induced enhancements of elastic constants, elastic moduli, elastic wave velocities, and Debye temperature of the fluorite phase are observed. Phonon spectrums of both the ground state fluorite structure and high pressure cotunnite structure calculated by the supercell approach show that the cotunnite structure is dynamically unstable under ambient pressure. Based on the imaginary mode along the  $\Gamma$ - $X$  direction and soft phonon mode along the  $\Gamma$ - $Z$  direction, a transition path from cotunnite to fluorite has been identified. We calculate the lattice vibrational energy in the quasiharmonic approximation using both first-principles phonon density of state and the Debye model. Calculated temperature dependence of lattice parameter, entropy, and specific heat agree well with experimental observations in the low temperature domain. The difference of Gibbs free energy between the two phases of  $\text{UO}_2$  has predicted a boundary in the pressure-temperature phase diagram. The solid-liquid boundary is approximated by an empirical equation using our calculated elastic constants.

PACS numbers: 71.27.+a, 61.50.Ks, 62.20.-x, 63.20.dk

## I. INTRODUCTION

Due to its critical importance in nuclear fuel cycle and complex electronic structure arisen from a partially occupied  $5f$  orbital, uranium dioxide ( $\text{UO}_2$ ) has been studied extensively in experiments [1–5] and computational simulations [6–14]. The  $5f$  electrons in  $\text{UO}_2$  play a pivotal role in understanding its electronic, thermodynamic, and magnetic properties [15]. Using conventional density functional theory (DFT) of exchange-correlation potential, i.e., the local density approximation (LDA) or generalized gradient approximation (GGA), an incorrect ferromagnetic (FM) conducting ground state of  $\text{UO}_2$  was observed [8] since an error produced by underestimating the strong on-site Coulomb repulsion of the  $5f$  electrons. Same problems have been confirmed in previous investigations of  $\text{NpO}_2$  [16] and  $\text{PuO}_2$  [13] within the pure LDA/GGA schemes. Fortunately, for  $\text{PuO}_2$  a theory based on completely localized  $5f$  states reproduced well the crystal field splittings as well as the magnetic susceptibility [17]. The  $f \rightarrow f$  antiferromagnetic (AFM) Mott-Hubbard insulator nature of  $\text{UO}_2$  has been well reproduced in LDA/GGA+ $U$  [7], hybrid density functional of (Heyd, Scuseria, and Enzerhof) HSE [10], self-interaction corrected local spin-density (SIC-LSD) [12],

and LDA plus Dynamical Mean-Field Theory (DMFT) [18] calculations to account for the photoelectron spectroscopy experiments [1, 2].

At ambient conditions,  $\text{UO}_2$  crystallizes in a cubic fluorite structure ( $Fm\bar{3}m$ , No. 225) with cations arranging in a face-centered cubic (fcc) structure and anions occupying tetrahedral sites. Similar to the high-pressure behavior of  $\text{ThO}_2$  and  $\text{PuO}_2$  [19], a recent hydrostatic compression experiment [3] has shown that  $\text{UO}_2$  also transforms to the orthorhombic structure of cotunnite-type ( $Pnma$ , No. 62) at room temperature, beyond 42 GPa. This kind of pressure-induced phase transition (PT) for actinide dioxides is the same as for the alkaline earth fluorides [20] and has not been sufficiently studied, although many experiments [3, 19] and theoretical works [13, 21, 22] have paid attentions on this issue. The cotunnite phase data are scarce in the literature, especially for its thermodynamic properties and vibrational characters. Temperature contributions to the PT have not been included in previous studies. On the other hand, the melting performances of  $\text{UO}_2$  also have not been well investigated. Only few experiments have been conducted to describe the melting features of  $\text{UO}_2$  near ambient pressure, because of the difficult experimental conditions required to control and monitor the PT [23].

In our previous systematic work [13], we have presented structural, electronic, and mechanical properties of AFM  $\text{UO}_2$  in its ground-state fluorite phase and high-pressure cotunnite phase at their corresponding equilibrium states within LDA+ $U$  formalism with  $U=4$  eV. The lattice parameter  $a_0=5.449$  Å and bulk modulus

\*E-mail: wbt11129@sxu.edu.cn

†E-mail: zhang\_ping@iapcm.ac.cn

‡E-mail: olle.eriksson@physics.uu.se

$B=220.0$  GPa for  $Fm\bar{3}m$   $UO_2$  obtained by the third-order Birch-Murnaghan equation of state (EOS) [24] fitting were found to be in perfect agreement with results of recent LDA+ $U$  calculation [25] ( $a_0=5.448$  Å and  $B=218$  GPa) and experiments [3, 26] ( $a_0=5.47$  Å and  $B=207$  GPa). In the present work, we perform an extended study of the structural, mechanical, and thermodynamic properties of  $UO_2$  in the pressure range from 0 to 250 GPa and in a temperature interval from 0 to 4000 K by employing the LDA+ $U$  and GGA+ $U$  schemes as implemented by Dudarev *et al.* [7, 27, 28]. The total energies of nonmagnetic (NM), AFM, and FM phases of the fluorite structure have been calculated in a wide range of the effective Hubbard  $U$  parameter within LDA/GGA+ $U$  schemes to guarantee the validity of the ground-state calculations. At 0 K, a  $Fm\bar{3}m \rightarrow Pnma$  PT pressure of 40 GPa is predicted. So, we have calculated the elastic constants, elastic moduli, Poisson's ratio, elastic wave velocities, and Debye temperature of AFM fluorite  $UO_2$  in the pressure range from 0 to 40 GPa. The structural transition path of cotunnite phase to fluorite phase as well as the melting behavior have been studied based upon our calculated phonon dispersions, Gibbs free energy, and elastic constants. Thermodynamic properties including of Gibbs free energy, temperature dependence of the lattice parameter and the bulk modulus, entropy, and specific heat have also been evaluated. The rest of this paper is arranged as follows. In Sec. II the computational methods are described. In Sec. III we present and discuss our results. In Sec. IV we summarize the conclusions of this work.

## II. COMPUTATIONAL METHODS

### A. Computational details

First-principles DFT calculations on the basis of the frozen-core projected augmented wave (PAW) method of Blöchl [29] are performed within the Vienna *ab initio* simulation package (VASP) [30], where the exchange and correlation effects are described by the LDA and GGA [31, 32]. For the plane-wave set, a cutoff energy of 500 eV is used. The  $k$ -point meshes in the full wedge of the Brillouin zone (BZ) are sampled by  $9 \times 9 \times 9$  and  $9 \times 15 \times 9$  grids according to the Monkhorst-Pack (MP) [33] scheme for fluorite and cotunnite  $UO_2$ , respectively, and all atoms are fully relaxed until the Hellmann-Feynman (HF) forces become less than  $0.02$  eV/Å. The U  $6s^2 7s^2 6p^6 6d^2 5f^2$  and the O  $2s^2 2p^4$  orbitals are treated as valence electrons. Similar to our previous studies [13, 16], the strong on-site Coulomb repulsion among the localized U  $5f$  electrons is described by using the LDA/GGA+ $U$  formalisms formulated by Dudarev *et al.* [7, 27, 28], where the double counting correction has already been included. In this paper the Coulomb  $U$  is treated as a variable, while the exchange energy is set to be a constant  $J=0.51$  eV. This value of  $J$  had been checked carefully by Dudarev *et al.*

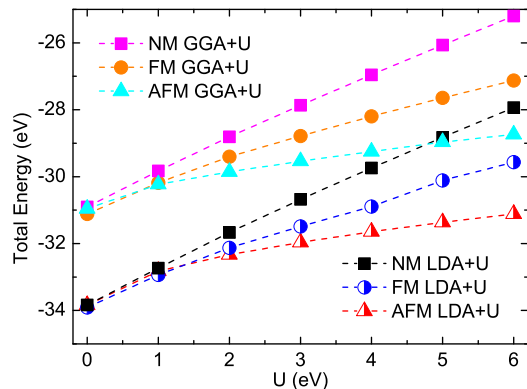


FIG. 1: (Color online) Dependence of the total energies (per formula unit) on  $U$  for NM, FM, and AFM  $UO_2$  in  $Fm\bar{3}m$  phase.

[7, 27, 28]. Since only the difference between  $U$  and  $J$  is significant [28], we will henceforth label them as one single parameter, for simplicity labeled as  $U$ , while keeping in mind that the non-zero  $J$  has been used during calculations.

Both spin-unpolarized and spin-polarized calculations are performed in this study. We show in Fig. 1 the dependence of the total energy (per formula unit at respective optimum geometries) on  $U$  for NM, FM, and AFM phases within the LDA+ $U$  and GGA+ $U$  formalisms. Clearly, the NM phase is not energetically favorable in the LDA+ $U$  and GGA+ $U$  formalisms, compared to FM and AFM phases. Therefore, the results of NM calculations are not presented in the following. At  $U=0$  and  $1.0$  eV, the total energy of the FM phase is lower than or almost equal to that of the AFM phase either in LDA+ $U$  scheme or GGA+ $U$  scheme. However, as shown in Fig. 1, it is clear that the total energy of the AFM phase decreases to become lower than that of the FM phase when increasing  $U$ . The total-energy differences ( $E_{FM} - E_{AFM}$ ) within the LDA+ $U$  and GGA+ $U$  at  $U=4$  eV are 0.755 and 1.053 eV, respectively. The AFM stable nature established by LDA+ $U$  or GGA+ $U$  scheme is consistent with experiments [2, 34, 35]. In the following study, we focus on results of the AFM phase. Also, although the spin-orbit coupling (SOC) is important for certain properties of heavy metal compounds, inclusion of SOC has limited effect on the bulk-properties and chemical binding of  $UO_2$  and  $PuO_2$  [8, 13, 36–39]. The reason for this is that the  $f$ -shell is localized in these compounds, and the chemical binding is provided by the  $spd$ -states of U and the  $sp$ -states of O, and for these states SOC is less important. Therefore, in our present work of  $UO_2$ , the SOC is not included.

## B. Elastic properties, Debye temperature, and melting temperature

To avoid the Pulay stress problem, the geometry optimization at each volume is performed at fixed volume rather than constant pressure. Elastic constants for cubic symmetry ( $C_{11}$ ,  $C_{12}$ , and  $C_{44}$ ) and orthorhombic structure ( $C_{11}$ ,  $C_{12}$ ,  $C_{13}$ ,  $C_{22}$ ,  $C_{23}$ ,  $C_{33}$ ,  $C_{44}$ ,  $C_{55}$ , and  $C_{66}$ ) are calculated by applying stress tensors with various small strains onto the equilibrium structures. The strain amplitude  $\delta$  is varied in steps of 0.006 from  $\delta=-0.036$  to 0.036. Detailed descriptions of calculation scheme please see our previous work [13]. After obtaining elastic constants, the polycrystalline bulk modulus  $B$  and shear modulus  $G$  are calculated from the Voigt-Reuss-Hill (VRH) approximations [40]. The Young's modulus  $E$  and Poisson's ratio  $\nu$  are calculated through  $E = 9BG/(3B + G)$  and  $\nu = (3B - 2G)/[2(3B + G)]$ . In calculation of the Debye temperature ( $\theta_D$ ), we use the relation

$$\theta_D = \frac{h}{k_B} \left( \frac{3n}{4\pi\Omega} \right)^{1/3} v_m, \quad (1)$$

where  $h$  and  $k_B$  are Planck and Boltzmann constants, respectively,  $n$  is the number of atoms in the molecule,  $\Omega$  is molecular volume, and  $v_m$  is the average sound wave velocity. The average wave velocity in the polycrystalline materials is approximately given as

$$v_m = \left[ \frac{1}{3} \left( \frac{2}{v_t^3} + \frac{1}{v_l^3} \right) \right]^{-1/3}, \quad (2)$$

where  $v_t = \sqrt{G/\rho}$  ( $\rho$  is the density) and  $v_l = \sqrt{(3B + 4G)/3\rho}$  are the transverse and longitudinal elastic wave velocity of the polycrystalline materials, respectively. The melting temperature ( $T_m$ ) in units of K for cubic  $\text{UO}_2$  are deduced from elastic constant ( $C_{11}$ ) by an approximate empirical linear formula [41]:

$$T_m = 553 + 5.91C_{11}, \quad (3)$$

where the  $C_{11}$  is in units of GPa and the standard error is about  $\pm 300$  K.

## C. Phonon and thermodynamic properties

We use the supercell approach [42] and the small displacement method as implemented in the FROPHO code [43] to calculate the phonon curves in the BZ and the corresponding phonon density of states (DOS) for both fluorite and cotunnite phases of  $\text{UO}_2$ . In the interpolation of the force constants for the phonon dispersion curve calculations,  $3 \times 3 \times 3$  and  $3 \times 5 \times 3$  MP  $k$ -point meshes are used for  $Fm\bar{3}m$   $2 \times 2 \times 2$  and  $Pnma$   $2 \times 2 \times 2$  supercells, respectively. The forces induced by small displacements are calculated within VASP.

Thermodynamic properties can be determined by phonon calculation using the quasiharmonic approximation (QHA) [13, 44] or by the quasiharmonic Debye model [45]. Within these two models, the Gibbs free energy  $G(T, P)$  is written as

$$G(T, P) = F(T, V) + PV. \quad (4)$$

Here,  $F(T, V)$  is the Helmholtz free energy at temperature  $T$  and volume  $V$  and can be expressed as

$$F(T, V) = E(V) + F_{vib}(T, V) + F_{el}(T, V), \quad (5)$$

where  $E(V)$  is the ground-state total energy,  $F_{vib}(T, V)$  is the vibrational energy of the lattice ions and  $F_{el}(T, V)$  is the thermal electronic contribution. Similar to our previous work [13],  $F_{el}(T, V)$  is also not included in present study.

Under QHA, the  $F_{vib}(T, V)$  can be calculated by

$$F_{vib}(T, V) = k_B T \int_0^\infty g(\omega) \ln \left[ 2 \sinh \left( \frac{\hbar\omega}{2k_B T} \right) \right] d\omega, \quad (6)$$

where  $\omega$  represents the phonon frequencies and  $g(\omega)$  is the phonon DOS. This formula requests positive results of the phonon DOS. So it is not suitable for dynamically unstable phases. Instead, the vibration energy for phases with imaginary phonon frequencies can be estimated by the Debye model

$$F_{vib}(T, V) = \frac{9}{8} k_B \theta_D + k_B T \left[ 3 \ln \left( 1 - e^{-\frac{\theta_D}{T}} \right) - D \left( \frac{\theta_D}{T} \right) \right], \quad (7)$$

where  $\frac{9}{8} k_B \theta_D$  is zero-point energy due to lattice ion vibration at 0 K and  $D(\theta_D/T)$  the Debye integral written as  $D(\theta_D/T) = 3/(\theta_D/T)^3 \int_0^{\theta_D/T} x^3/(e^x - 1) dx$ . For a more detailed computation scheme of the Debye model please see Ref. [45].

## III. RESULTS

### A. Phase transition at 0 K

In the present study, the structural parameter and bulk modulus for  $Fm\bar{3}m$  AFM  $\text{UO}_2$  calculated using LDA+ $U$  formalism with  $U=4$  eV are identical to our previous results [13]. The insulating energy band gap ( $E_g$ ) and spin moment per U atom ( $\mu_{mag.}$ ) are calculated to be 1.9 eV and  $1.977 \mu_B$ , respectively, which are in good agreement with previous LDA+ $U$  calculation [21] ( $E_g=1.45$  eV and  $\mu_{mag.}=1.93 \mu_B$ ) and experiments ( $E_g=2.0$  eV [2] and  $\mu_{mag.}=1.74 \mu_B$  [35]). For  $Pnma$   $\text{UO}_2$  in AFM phase, we obtain the optimized structural lattice parameters  $a$ ,  $b$ , and  $c$  to be 5.974, 3.604, and 6.967 Å, respectively, after fitting the energy-volume data to the EOS. Band gap and spin moment are calculated to be 1.6 eV and  $2.002 \mu_B$ , respectively. Thus, the band gaps should not increase from  $Fm\bar{3}m$  phase to  $Pnma$  phase when using

TABLE I: Lattice constants, elastic constants, various moduli, Poisson's ratio ( $\nu$ ), density ( $\rho$ ), transverse ( $\nu_t$ ), longitudinal ( $\nu_l$ ) and average ( $\nu_m$ ) sound velocities, and Debye temperature ( $\theta_D$ ) for  $Fm\bar{3}m$  AFM  $UO_2$  at different pressures calculated within LDA+ $U$  formalism with  $U=4$  eV. For comparison, experimental values and other calculation results at 0 GPa are also listed.

Pressure (GPa)	a (Å)	$C_{11}$ (GPa)	$C_{12}$ (GPa)	$C_{44}$ (GPa)	$B$ (GPa)	$G$ (GPa)	$E$ (GPa)	$\nu$	$\rho$ (g/cm <sup>3</sup> )	$\nu_t$ (m/s)	$\nu_l$ (m/s)	$\nu_m$ (m/s)	$\theta_D$ (K)
0	5.449	389.3	138.9	71.3	222.4	89.5	236.8	0.323	11.084	2841.8	5552.7	3183.4	398.1
5	5.408	414.8	154.5	94.3	241.2	107.3	280.4	0.306	11.343	3076.1	5821.1	3438.7	433.3
10	5.373	438.2	166.7	106.7	257.2	117.5	305.9	0.302	11.565	3187.5	5982.3	3561.2	451.7
15	5.340	459.2	181.6	118.9	274.1	126.5	328.9	0.300	11.776	3277.7	6131.8	3661.1	467.2
20	5.310	479.8	195.6	131.3	290.4	135.5	351.8	0.298	11.979	3363.3	6270.7	3755.8	482.0
25	5.282	500.3	208.3	143.6	305.6	144.6	374.6	0.296	12.175	3445.7	6398.0	3846.7	496.3
30	5.254	520.8	221.6	156.0	321.3	153.4	397.0	0.294	12.364	3522.3	6521.7	3931.4	509.8
35	5.229	540.0	233.7	167.8	335.8	161.8	418.2	0.292	12.546	3591.1	6630.0	4007.3	522.2
40	5.204	558.0	246.7	180.9	350.4	170.3	439.8	0.291	12.722	3659.1	6737.7	4082.5	534.5
Expt.	5.4731 <sup>a</sup>	389.3 <sup>b</sup>	118.7 <sup>b</sup>	59.7 <sup>b</sup>	209.0 <sup>b</sup>	83.0 <sup>b</sup>	221.0 <sup>b</sup>	0.324 <sup>b</sup>					385 <sup>b</sup> , 395 <sup>c</sup>
LDA+ $U^d$	5.448	380.9	140.4	63.2	220.6	82.0	218.9	0.335					399

<sup>a</sup> Reference [3], <sup>b</sup> Reference [46], <sup>c</sup> Reference [49], <sup>d</sup> Reference [39].

same value of Hubbard parameters. This is different from previous LDA+ $U$  calculation [21], where an increase of the band gap was found at a cell volume close to the transition pressure from 0.8 eV in the fluorite phase to 2.4 eV in the cotunnite phase, by using different values of Hubbard parameters. Although the PT behaviors should seek help from larger value of Hubbard  $U$  parameter (see follows), we present equilibrium state properties of  $Pnma$   $UO_2$  with  $U=4$  eV.

In Fig. 2, we show the total energy vs cell volume curves since their critical role in solid-state behavior descriptions. Because the pressure induced PT can not be properly modeled by  $U=4$  eV within LDA+ $U$ , we calculate the energy-volume data of  $Pnma$  phase by  $U=5.5$  eV. Detailed explanation on this issue can be found in Ref. [21]. It is clear that the  $Fm\bar{3}m$  phase is stable under ambient condition and upon compression it will transit to the  $Pnma$  phase. At 0 K, the Gibbs free energy is equal to the enthalpy  $H$ . After calculation, we can plot in Fig. 2 (see the inset) the relative enthalpies of the  $Pnma$  phase with respect to the  $Fm\bar{3}m$  phase as a function of pressure. The cross point predict a PT pressure of 40 GPa, which is consistent with previous LDA+ $U$  calculation [21] value of  $\sim 38$  GPa and also the experimentally observed 42 GPa [3].

## B. Elasticity of fluorite $UO_2$

Elastic constants can measure the resistance and mechanical features of crystal to external stress or pressure, thus describing the stability of crystals against elastic deformation. We present in Table I the lattice constants, elastic constants, bulk moduli, shear moduli, Young moduli, Poisson's ratio, density, elastic wave velocities, and Debye temperature for  $Fm\bar{3}m$  AFM  $UO_2$

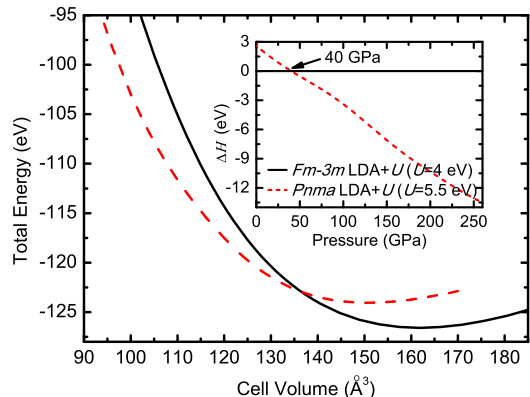


FIG. 2: (Color online) Total energy vs the cell volume for AFM  $UO_2$  in  $Fm\bar{3}m$  and  $Pnma$  phases. Results of  $Fm\bar{3}m$  are calculated within LDA+ $U$  formalism with  $U=4$  eV, while for  $Pnma$  phase are obtained by  $U=5.5$  eV. A PT at 40 GPa is predicted by the pressure dependence of the enthalpy differences of  $Pnma$  phase with respect to  $Fm\bar{3}m$  phase, as shown in the inset.

at different pressures. All these results are calculated within the LDA+ $U$  formalism with  $U=4$  eV. The values at zero pressure is the same as in our previous work [13]. Actually, elastic constants at 0 GPa have been widely studied either by experiments [46] or by calculations [39, 47, 48]. Our calculated results at 0 GPa are consistent with corresponding values from experiments [46] and recent LDA+ $U$  work [39], where Sanati *et al.* have presented carefully discussions on the zero pressure results. In this study, various moduli, Poisson's ratio ( $\nu$ ), density ( $\rho$ ), elastic wave velocities ( $\nu_t$ ,  $\nu_l$ , and  $\nu_m$ ), and Debye temperature ( $\theta_D$ ) of low-pressure fluorite phase  $UO_2$  in the pressure range from 0 GPa to 40 GPa have

been deduced from elastic constants. In the entire pressure range,  $C_{11}$  is prominently larger than  $C_{12}$ , indicating that the bonding strength along the  $[100]/[010]/[001]$  directions is clearly stronger than that of the bonding along the  $[011]/[101]/[110]$  directions. In fact, there are eight U–O covalent bonds per formula unit for fluorite  $\text{UO}_2$ . The angle of all eight bonds with respect to the  $[100]/[010]/[001]$  directions is  $45^\circ$ . However, only four bonds make an angle of  $45^\circ$  with the  $[011]/[101]/[110]$  directions. Four other bonds are vertical to the strain directions of  $[011]/[101]/[110]$ . The bonds vertical to the strain directions have no contributions on the elastic strength. Therefore, the fact that  $C_{11} > C_{12}$  for cubic  $\text{UO}_2$  is understandable. This kind of bonding analysis has been used previously to explain the different theoretical tensile strengths in the three typical crystalline orientations of  $\text{PuO}_2$  [13]. For the Debye temperature, our calculated result of 398.1 K is in excellent agreement with experiments [46, 49].

As indicated in Table I, except poisson's ratio, pressure-induced enhancements of elastic constants, elastic moduli, elastic wave velocities, and Debye temperatures are evident. They all increase linearly with pressure. While  $C_{12}$  and  $C_{44}$  have the same increase rate of  $\sim 2.7$ ,  $C_{11}$  has a larger one of  $\sim 4.2$ . This also can be understood from the previous bonding analysis. The rates with which  $B$ ,  $G$ , and  $E$  increase, are 3.2, 2.0, and 5.1, respectively. Considering  $B_V = B_R = (C_{11} + 2C_{12})/3$ ,  $G_V = (C_{11} - C_{12} + 3C_{44})/5$ , and  $G_R = 5(C_{11} - C_{12})C_{44}/[4C_{44} + 3(C_{11} - C_{12})]$  for cubic symmetry, we can understand the fact that the increase rate of  $G$  is only about 60% of the increase rates of  $B$ . For  $v_t$  and  $v_l$ , increase rates of 20.4 and 29.6 m/s/GPa are obtained, respectively. Relatively larger increase rate of transverse sound velocity upon compression is due to the larger enhancement of the bulk modulus  $B$  with respect to the shear modulus  $G$ . The pressure-dependent linearly increasing behavior of Debye temperature is also clear. This kind of analysis for Debye temperature should supply useful informations in practical application and/or theoretical analysis for  $\text{UO}_2$ .

### C. Phonon dispersion

The calculated phonon dispersion curves as well as corresponding phonon DOSs are displayed in Fig. 3 for  $Fm\bar{3}m$  and  $Pnma$   $\text{UO}_2$  in the AFM configuration. To our knowledge, no experimental or theoretical phonon frequency results have been published for the high-pressure phase of actinide dioxides. For  $Fm\bar{3}m$   $\text{UO}_2$ , inelastic neutron scattering [49], infrared and Raman spectroscopic [1, 50, 51] experiments as well as LDA+DMFT [11], MD [52], and LDA/GGA+ $U$ +SOC [39] calculations have been performed to picture its vibrational features. In addition to their phonon curves along  $\langle 001 \rangle$ ,  $\langle 110 \rangle$ , and  $\langle 111 \rangle$  directions in the BZ, we have shown phonon dispersions along  $\Gamma-X-K-\Gamma-L-X-W$

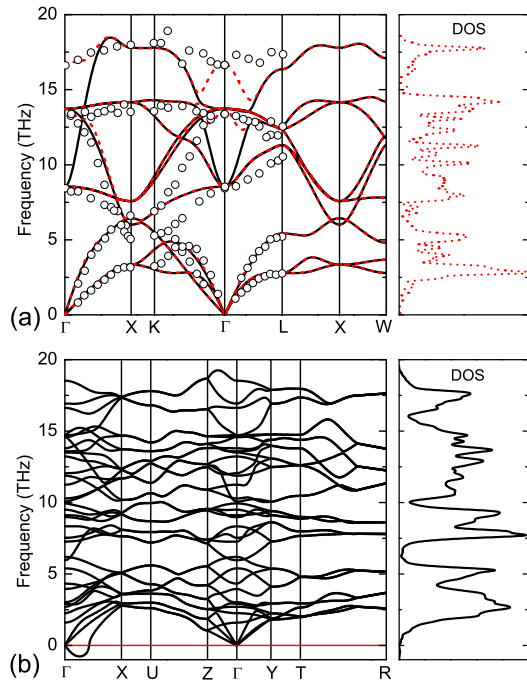


FIG. 3: (Color online) Phonon dispersion curves (left panel) and corresponding phonon DOS (right panel) for  $\text{UO}_2$  in (a)  $Fm\bar{3}m$  phase and (b)  $Pnma$  phase. All results are calculated within LDA+ $U$  formalism with  $U=4$  eV. The solid lines are calculated without including the polarization effects, while the dashed lines including. The hollow circles present the experimental data from Ref. [49].

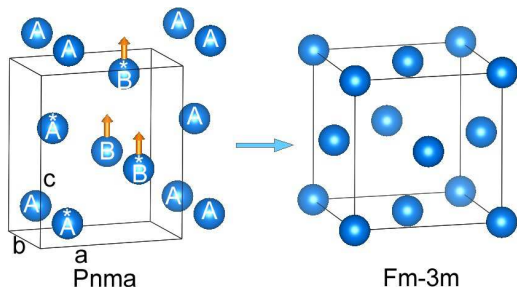


FIG. 4: (Color online) Schematic illustrations of the structural transition from  $Pnma$  phase to  $Fm\bar{3}m$  structure. For clarity, only uranium atoms are presented and atoms within the  $Pnma$  unit cell are labeled by star symbols.

directions. The  $\Gamma-X$ ,  $\Gamma-K$ , and  $\Gamma-L$  lines are along  $\langle 001 \rangle$ ,  $\langle 110 \rangle$ , and  $\langle 111 \rangle$  directions, respectively. As having been demonstrated by Sanati *et al.* [39], including of SOC does not significantly modify the phonon DOSs and the contribution of the lattice distortion is also limited, however, when Hubbard corrections are not included, the higher-frequency phonon modes are shifted to lower frequencies and the optical modes are underestimated. Therefore, we have calculated phonon dis-

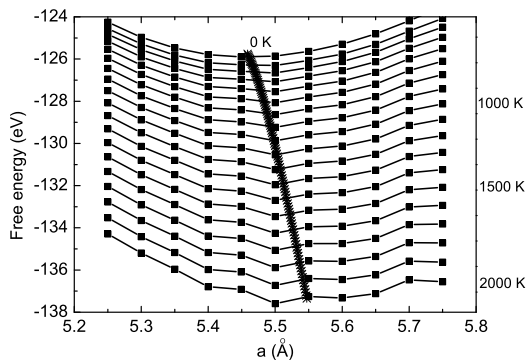


FIG. 5: Dependence of the free energy  $F(T, V)$  on crystal lattice parameter  $a$  for a number of selected temperatures for AFM  $\text{UO}_2$  calculated within LDA+ $U$  formalism with  $U=4$  eV.

persions and phonon DOSs of cubic  $\text{UO}_2$  by LDA+ $U$  scheme without including SOC. From Fig. 3(a), one can find that including polarization effect is necessary to correctly account for the LO-TO splitting near the  $\Gamma$  point in BZ. Here, the Born effective charges ( $Z_{\text{U}}^*=5.54$  and  $Z_{\text{O}}^*=-2.77$ ) of U and O ions for  $Fm\bar{3}m$  AFM  $\text{UO}_2$  are also calculated. Our phonon dispersions are overall in good agreement with the inelastic neutron scattering experiment [49] and previous calculations [11, 39, 52].

As for  $Pnma$   $\text{UO}_2$ , we have shown phonon dispersions along  $\Gamma-X-U-Z-\Gamma-Y-T-R$  directions. The notations of the high-symmetry points are  $\Gamma$  (0, 0, 0),  $X$  (0,  $\frac{1}{2}$ , 0),  $U$  (0,  $\frac{1}{2}$ ,  $\frac{1}{2}$ ),  $Z$  (0, 0,  $\frac{1}{2}$ ),  $Y$  ( $-\frac{1}{2}$ , 0, 0),  $T$  ( $-\frac{1}{2}$ , 0,  $\frac{1}{2}$ ), and  $R$  ( $-\frac{1}{2}$ ,  $\frac{1}{2}$ ,  $\frac{1}{2}$ ). Although mechanically stable nature of  $Pnma$   $\text{UO}_2$  at its equilibrium state has been predicted by the elastic constants in our previous work [13], Fig. 3(b) clearly shows that the transverse acoustic (TA) mode close to  $\Gamma$  point becomes imaginary along the  $\Gamma-X$  (i.e., the  $\langle 010 \rangle$ ) direction. This means that the high-pressure phase of  $\text{UO}_2$  is dynamically unstable under ambient pressure. In addition, we can find a clear soft phonon mode along  $\Gamma-Z$  (i.e., the  $\langle 001 \rangle$ ) direction. Thus, uranium atoms in  $Pnma$  structure are easy to move along  $\langle 010 \rangle$  and  $\langle 001 \rangle$  directions. Based upon these observations, we show in Fig. 4 a suggested path of the  $Pnma \rightarrow Fm\bar{3}m$  transition. The  $Pnma$  phase can be viewed as an AB periodically layered structure along the [100] direction. In transition, firstly the adjacent (100) planes slip relatively along the [001] direction to create a face centered orthorhombic structure (as indicated by the arrows in Fig. 4), and second, the cell expands along the [010] direction and shrinks in the vertical directions to form the fcc fluorite structure.

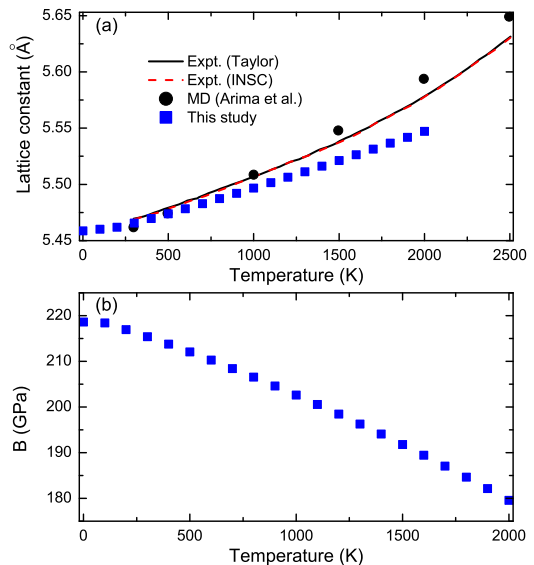


FIG. 6: (Color online) Temperature dependences of (a) lattice parameter  $a(T)$  and (b) bulk modulus  $B(T)$  of  $\text{UO}_2$ . Experimental results from [53] and [54] as well as the MD results from [55] are also shown in panel (a).

#### D. Thermodynamic properties and $P-T$ phase diagram

Calculated free energy  $F(T, V)$  curves of  $\text{UO}_2$  for temperatures ranging from 0 up to 2000 K are shown in Fig. 5. Note that in the calculation of  $F(T, V)$ , the ground-state total energy and phonon free energy should be calculated by constructing several  $2 \times 2 \times 2$  fcc super-cells. This kind of calculation is computationally very expensive. In Fig. 5, the equilibrium lattice parameters at different temperature  $T$  are also presented. The equilibrium volume  $V(T)$  and the bulk modulus  $B(T)$  are obtained by EOS fitting. Figure 6 shows the temperature dependence of the lattice parameter and the bulk modulus. Experimental results from [53] and [54] as well as the MD results from [55] are also plotted. We observe good agreement of calculated lattice parameters with respect to the experiments in the low temperature domain, but somewhat lower values compared to experiments in temperature higher than 800 K. The differences may come from the thermal electronic contribution and/or anharmonic effects. For the bulk modulus  $B(T)$ , similar as for  $\text{PuO}_2$  [13], a decreasing behavior upon elevating temperature is observed. The decreasing amplitude of  $B(T)$  from 0 K to 1500 K for  $\text{UO}_2$  is  $\sim 26.8$  GPa, which is larger than that of  $\text{PuO}_2$  by about 6.2 GPa. This means that  $\text{UO}_2$  will be softened quicker upon increasing temperature in comparison with  $\text{PuO}_2$ .

Using QHA and the Debye model, we have calculated the Gibbs free energy ( $G$ ), entropy ( $S$ ), and specific heat at constant volume ( $C_V$ ) for  $Fm\bar{3}m$  and  $Pnma$  phases of  $\text{UO}_2$ . Since the specific heat at constant pressure ( $C_P$ )

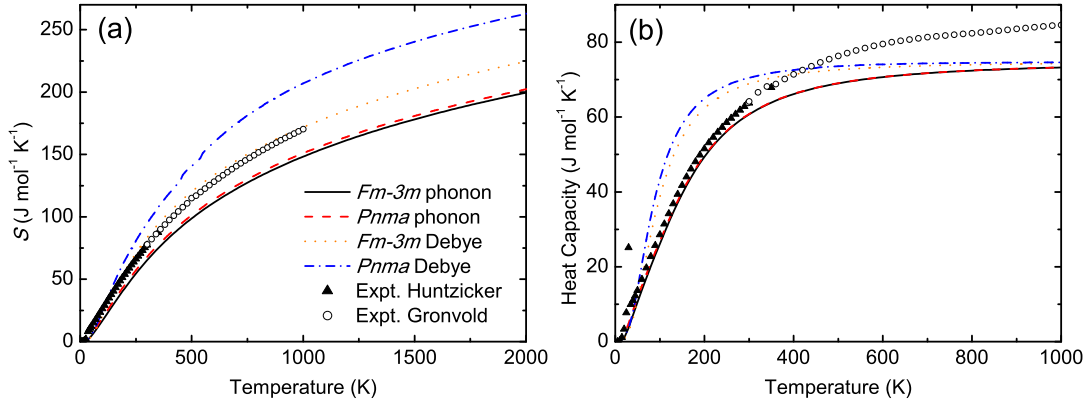


FIG. 7: (Color online) Temperature dependences of (a) entropy and (b) heat capacity at constant volume,  $C_V$ , for  $\text{UO}_2$  in  $Fm\bar{3}m$  and  $Pnma$  phases at 0 GPa. Results of QHA and Debye are presented together with experimental values from [56] and [57].

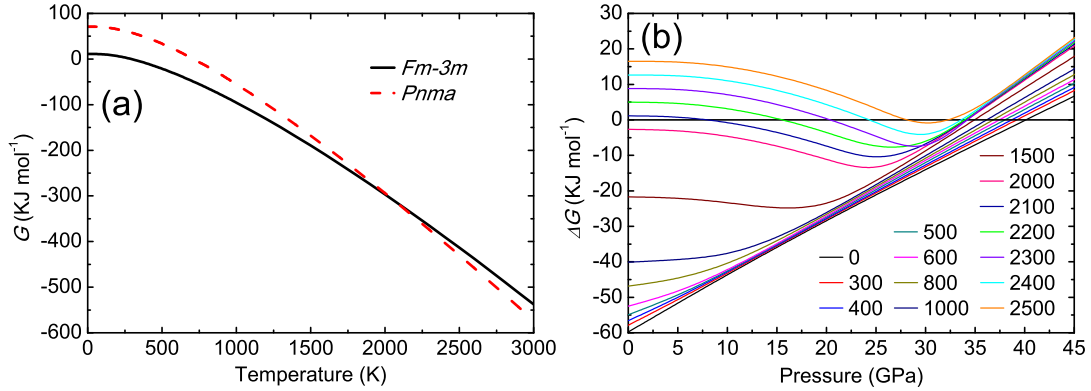


FIG. 8: (Color online) (a) Temperature dependences of Gibbs free energy curves for  $\text{UO}_2$  in  $Fm\bar{3}m$  and  $Pnma$  phases at 0 GPa. (b) The difference of the Gibbs free energies of the  $Fm\bar{3}m$  and  $Pnma$  phases of  $\text{UO}_2$  as a function of pressure for several temperatures (in K). A positive value indicates that the  $Pnma$  phase is more stable.

is similar to  $C_V$  [13], we will not present  $C_P$  results in this work. Entropy and heat capacity at constant volume results at 0 GPa are presented in Fig. 7 and Gibbs free energy results are plotted in Fig. 8. Experimental results [56, 57] of  $S$  and  $C_V$  are also showed for comparison. Under QHA, the entropy  $S$  curves for  $Fm\bar{3}m$  and  $Pnma$  phases are almost identical to each other. Similar to previous calculation [39], the  $S$  of fluorite  $\text{UO}_2$  is underestimated in a wide range of temperatures with respect to experiments. However, as clearly indicated in Fig. 7(a), the Debye model can give proper results for  $Fm\bar{3}m$   $\text{UO}_2$ . Using the Debye model, the  $S$  curves for  $Fm\bar{3}m$  and  $Pnma$  phases will separate along with increasing temperature. The difference between QHA and Debye model is due to the fact that QHA uses harmonic approximation and the Debye model has considered some anharmonic contributions in calculations of  $S$  and  $C_V$ . Although the Debye model is less accurate, it can supply a qualitative picture or even quantitative description of the thermodynamic properties. As shown in Fig. 7(b),

the  $C_V$  of  $Fm\bar{3}m$   $\text{UO}_2$  under QHA agrees well with experiments up to room temperature and becomes close to a constant of the Dulong-Petit limit [58]. Same trends of  $C_V$  curve for  $Fm\bar{3}m$  phase has been observed by Sanati *et al.* [39] and our results based on phonon DOS indicate that the  $C_V$  curves for  $Fm\bar{3}m$  and  $Pnma$  phases are almost identical to each other. However, under the Debye model, slower increasing behavior of  $Fm\bar{3}m$  phase  $C_V$  with increasing temperature is observed with respect to the  $Pnma$  phase. The Debye model gives  $\theta_D=390.6$  and  $352.8$  K for  $Fm\bar{3}m$  and  $Pnma$  phases, respectively, which are in good agreement with  $398.1$  and  $343.7$  K [13] computed by elastic constants.

As shown in Fig. 8(a), the cross between  $Fm\bar{3}m$  and  $Pnma$  phases Gibbs free energy curves of  $\text{UO}_2$  by Debye calculations, readily gives a  $Fm\bar{3}m \rightarrow Pnma$  phase transition temperature of 2069 K. This implies a significant temperature contribution for the  $Fm\bar{3}m \rightarrow Pnma$  phase transition, which is not only pressure driven. To predict the phase boundary of  $Fm\bar{3}m \rightarrow Pnma$ , we calculate here

the Gibbs free energy of the  $Fm\bar{3}m$  and  $Pnma$  crystal structures in a temperature range from 0 to 3000 K, and the pressure effect is studied in the range of 0 to 45 GPa. The Gibbs energy difference between the fluorite and cotunnite structures ( $\Delta G$ ) of  $UO_2$  as a function of pressure for several temperatures is reported in Fig. 8(b). At 0 K, the  $Fm\bar{3}m \rightarrow Pnma$  PT pressure is predicted to be 40 GPa, which is identical to our aforementioned result. Along with increasing temperature in the range from 0 to 2069 K, the pressure of the  $Fm\bar{3}m \rightarrow Pnma$  transition decreases slightly. At higher temperatures, the  $Fm\bar{3}m$  phase is only stable in middle pressure range.

Once the free energies of the two experimentally observed structures are determined, the phase boundary can be obtained by equating Gibbs free energies at a given pressure and temperature. Besides, the solid-liquid boundary can be featured by the melting temperature  $T_m$ . Based on these results, we can plot in Fig. 9 the phase diagram of  $UO_2$ . Other theoretical [21, 55] and experimental [3, 23] values are also presented for comparison. For the phase boundary between  $Fm\bar{3}m$  and  $Pnma$ , only one point at ambient condition was reported in experiment. Our predicted results call for further experimental and theoretical works, to investigate the accuracy of the theory. For the solid-liquid boundary, the experimentally determined melting value at zero pressure is 3147 K [23]. We note that experiment and recent MD calculation have reported the relationship between melting point and pressure to be  $T_{m,P} = 3147 + 92.9P$  and  $T_{m,P} = 3178 + 115P$ , respectively, where  $P$  is pressure in unit of GPa. Using our calculated data in Fig. 9, we obtain  $T_{m,P} = 2882 + 24.8P$ . The melting point at zero pressure is underestimated by about 265 K, which is the same with previous LDA+ $U$  calculation [39]. The increasing rate of  $T_{m,P}$  is largely underestimated compared to experiment. Although we do not wish to state that our calculations are more reliable than experiment, it stands clear that since the experiment was performed in a narrow range of pressure between 0.01 and 0.25 GPa, the differences between our calculation and previous experiment call for more theoretical and experimental works.

#### IV. CONCLUSION

In summary, we have carried out a first-principles DFT+ $U$  exploration of the ground state properties as well as the high temperature/pressure behaviors of  $UO_2$ . By choosing the Hubbard  $U$  parameter around 4 eV within the LDA+ $U$  approach, the equilibrium state features for both the ambient  $Fm\bar{3}m$  and the high-pressure  $Pnma$  phases of  $UO_2$  are shown to agree well with experiments. The  $Fm\bar{3}m \rightarrow Pnma$  transition is predicted to occur at 40 GPa upon compression at 0 K. At ambient pressure, a transition temperature of 2069 K between the two solid structures is first obtained by the Debye

model. Pressure-dependent linearly increasing behaviors of mechanical properties and Debye temperature of fluo-

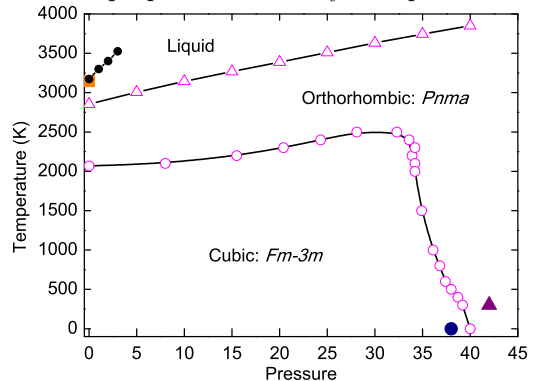


FIG. 9: (Color online) Calculated  $P$ - $T$  phase diagram for uranium dioxide compared with selected experimental points (square for melt point [23] and triangle for PT pressure [3]) and other calculations (line plus small solid circles for MD [55] and large circle for LDA+ $U$  [21]).

rite phase have been observed by calculating elastic constants. As a result, the melting temperature  $T_m$  also increases linearly with pressure. Phonon dispersion results of the  $Fm\bar{3}m$  phase are in good agreement with available experimental values. The LO-TO splitting at the  $\Gamma$  point is successfully reproduced by including the polarization effects. For the cotunnite phase, the imaginary mode along  $\Gamma-X$  direction and soft phonon mode along  $\Gamma-Z$  direction have been found at the equilibrium volume. The cotunnite to fluorite transition can be reached by firstly slipping the adjacent (100) planes relatively along the [001] direction to create a face-centered orthorhombic structure and secondly expanding the cell along the [010] direction and shrinking in the vertical directions to form the fcc fluorite structure. Using QHA and the Debye model, we have calculated the Gibbs free energy, temperature dependences of lattice parameter and bulk modulus, entropy, specific heat, and  $P$ - $T$  phase diagram of the important nuclear fuel material  $UO_2$ .

#### Acknowledgments

This work was supported by NSFC under Grant Nos. 11104170, 51071032, and 11074155, the Foundations for Development of Science and Technology of China Academy of Engineering Physics under Grant No. 2009B0301037. O.E. acknowledges support from the Swedish research council, the KAW foundation, ESSENCE, STANDUPP, and the ERC (project 247062 - ASD).



- 
- [1] J. Schoenes, Phys. Rep. **63**, 301 (1980).
- [2] Y. Baer and J. Schoenes, Solid State Commun. **33**, 885 (1980).
- [3] M. Idiri, T. Le Bihan, S. Heathman, and J. Rebizant, Phys. Rev. B **70**, 014113 (2004).
- [4] J. G. Tobin and S. W. Yu, Phys. Rev. Lett. **107**, 167406 (2011).
- [5] Y. Q. An, A. J. Taylor, S. D. Conradson, S. A. Trugman, T. Durakiewicz, and G. Rodriguez, Phys. Rev. Lett. **106**, 207402 (2011).
- [6] M. S. S. Brooks and P. J. Kelly, Solid State Commun. **45**, 689 (1983).
- [7] S. L. Dudarev, M. R. Castell, G. A. Botton, S. Y. Savrasov, C. Muggelberg, G. A. D. Briggs, A. P. Sutton, and D. T. Goddard, Micron **31**, 363 (2000).
- [8] C. E. Boettger and A. K. Ray, Int. J. Quantum Chem. **90**, 1470 (2002).
- [9] K. N. Kudin, G. E. Scuseria, and R. L. Martin, Phys. Rev. Lett. **89**, 266402 (2002).
- [10] I. D. Prodan, G. E. Scuseria, and R. L. Martin, Phys. Rev. B **76**, 033101 (2007).
- [11] Q. Yin and S. Y. Savrasov, Phys. Rev. Lett. **100**, 225504 (2008).
- [12] L. Petit, A. Svane, Z. Szotek, W. M. Temmerman, and G. M. Stocks, Phys. Rev. B **81**, 045108 (2010).
- [13] P. Zhang, B.-T. Wang, and X.-G. Zhao, Phys. Rev. B **82**, 144110 (2010).
- [14] H. Y. Geng, H. X. Song, K. Jin, S. K. Xiang, and Q. Wu, Phys. Rev. B **84**, 174115 (2011).
- [15] P. Santini, S. Carretta, G. Amoretti, R. Caciuffo, N. Magnani, and G. H. Lander, Rev. Mod. Phys. **81**, 807 (2009).
- [16] B. T. Wang, H. Shi, W. D. Li, and P. Zhang, Phys. Rev. B **81**, 045119 (2010).
- [17] M. Colarieti-Tosti, O. Eriksson, L. Nordstrom, J. M. Wills, and M. S. S. Brooks, Phys. Rev. B **65**, 195102 (2002).
- [18] Q. Yin, A. Kutepov, K. Haule, G. Kotliar, S. Y. Savrasov, and W. E. Pickett, Phys. Rev. B **84**, 195111 (2011).
- [19] J. P. Dancausse, E. Gering, S. Heathman, and U. Benedict, High Press. Res. **2**, 381 (1990).
- [20] S. M. Dorfman, F. Jiang, Z. Mao, A. Kubo, Y. Meng, V. B. Prakapenka, and T. S. Duffy, Phys. Rev. B **81**, 174121 (2010).
- [21] H. Y. Geng, Y. Chen, Y. Kaneta, and M. Kinoshita, Phys. Rev. B **75**, 054111 (2007).
- [22] B. T. Wang, H. Shi, W. D. Li, and P. Zhang, J. Nucl. Mater. **399**, 181 (2010).
- [23] D. Manara, C. Ronchi, M. Sheindlin, M. Lewis, and M. Brykin, J. Nucl. Mater. **342**, 148 (2005).
- [24] F. Birch, Phys. Rev. **71**, 809 (1947).
- [25] D. A. Andersson, J. Lezama, B. P. Uberuaga, C. Deo, and S. D. Conradson, Phys. Rev. B **79**, 024110 (2009).
- [26] T. Yamashita, N. Nitani, T. Tsuji, and H. Inagaki, J. Nucl. Mater. **247**, 90 (1997).
- [27] S. L. Dudarev, D. N. Manh, and A. P. Sutton, Philos. Mag. B **75**, 613 (1997).
- [28] S. L. Dudarev, G. A. Botton, S. Y. Savrasov, C. J. Humphreys, and A. P. Sutton, Phys. Rev. B **57**, 1505 (1998).
- [29] P. E. Blöchl, Phys. Rev. B **50**, 17953 (1994).
- [30] G. Kresse and J. Furthmüller, Phys. Rev. B **54**, 11169 (1996).
- [31] W. Kohn, L. J. Sham, Phys. Rev. **140** (1965) A1133.
- [32] J. P. Perdew, K. Burke, and Y. Wang, Phys. Rev. B **54**, 16533 (1996).
- [33] H. J. Monkhorst and J. D. Pack, Phys. Rev. B **13**, 5188 (1972).
- [34] J. Faber, G. H. Lander, and B. R. Cooper, Phys. Rev. Lett. **35**, 1770 (1975).
- [35] J. Faber and G. H. Lander, Phys. Rev. B **14**, 1151 (1976).
- [36] I. D. Prodan, G. E. Scuseria, and R. L. Martin, Phys. Rev. B **73**, 045104 (2006).
- [37] I. D. Prodan, G. E. Scuseria, J. A. Sordo, K. N. Kudin, and R. L. Martin, J. Chem. Phys. **123**, 014703 (2005).
- [38] C. E. Boettger and A. K. Ray, Int. J. Quantum Chem. **80**, 824 (2000).
- [39] M. Sanati, R. C. Albers, T. Lookman, A. Saxena, Phys. Rev. B **84**, 014116 (2011).
- [40] R. Hill, Phys. Phys. Soc. London **65**, 349 (1952).
- [41] M. E. Fine, L. D. Brown, and H. L. Marcus, Scr. Metall. **18**, 951 (1984).
- [42] K. Parlinski, Z.-Q. Li, and Y. Kawazoe, Phys. Rev. Lett. **78**, 4063 (1997).
- [43] A. Togo, F. Oba, and I. Tanaka, Phys. Rev. B **78** (2008) 134106.
- [44] A. Siegel, K. Parlinski, and U. D. Wdowik, Phys. Rev. B **74**, 104116 (2006).
- [45] A. A. Blanco, E. Francisco, and V. Luana, Comput. Phys. Commun. **158** (2004) 57.
- [46] I. J. Fritz, J. Appl. Phys. **47**, 4353 (1976).
- [47] S. L. Dudarev, G. A. Botton, S. Y. Savrasov, Z. Szotek, W. M. Temmerman, and A. P. Sutton, Phys Status Solidi, **166** 429 (1998).
- [48] A. J. Devey, J. Nucl. Mater. **412**, 301 (2011).
- [49] G. Dolling, R. A. Cowley, and A. D. B. Woods, Can. J. Phys. **43**, 1397 (1965).
- [50] T. Livneh and E. Sterer, Phys. Rev. B **73**, 085118 (2006).
- [51] T. Livneh, J. Phys.: Condens. Matter **20**, 085202 (2008).
- [52] P. Goel, N. Choudhury, and S. L. Chaplot, J. Nucl. Mater. **377**, 438 (2008).
- [53] D. Taylor, Br. Ceram. Trans. J. **83**, 32 (1984).
- [54] International Nuclear Safety Centre (INSC), Material Properties Database, Argonne National Laboratory, Illinois, USA, <http://www.insc.anl.gov/matprop/>.
- [55] T. Arima, K. Idemitsu, Y. Inagaki, Y. Tsujita, M. Kinoshita, and E. Yakub, J. Nucl. Mater. **389**, 149 (2009).
- [56] F. Grønvoold, N. J. Kveseth, A. Sveen, and J. Tichý, J. Chem. Thermodyn. **2**, 665 (1970).
- [57] J. J. Huntzicker and E. F. Westrum, J. Chem. Thermodyn. **3**, 61 (1971).
- [58] C. Kittel, *Introduction to Solid State Physics*, 7th ed. (Wiley, New York, 1996).